Supporting information

Coupling NiCo catalyst with carbon quantum dots on hematite photoanode for highly efficient oxygen evolution

Bin Zhao[a,b], Chenchen Feng[a], Xiaojuan Huang[a], Yong Ding[c] and Yingpu Bi*[a]

[a]State Key Laboratory for Oxo Synthesis & Selective Oxidation, National Engineering Research Center for Fine Petrochemical Intermediates, Lanzhou Institute of Chemical Physics, CAS, Lanzhou, Gansu 730000, China.

[b]University of Chinese Academy of Sciences, Beijing 100049, China.

[c]State Key Laboratory of Applied Organic Chemistry, Key Laboratory of Nonferrous Metals Chemistry and Resources Utilization of Gansu Province, and College of Chemistry and Chemical Engineering, Lanzhou University, Lanzhou, Gansu 730000, China.

Corresponding authors

E-mail: yingpubi@licp.cas.cn (Yingpu Bi).

1. Experimental section

Synthesis of carbon quantum dots (CDs)

CDs were prepared by a simple one-step microwave heating method.[1,2] 15.6 mmol citric acid and 16.7 mmol urea were completely dissolved in 10 mL water with vigorously stirred to form a transparent solution, then transferred to a microwave reactor and heated at 600 W for 10 min. After that, the transparent solution changed from colorless to brown-black porous solid. Subsequently, the spongy solid was ultrasonically dispersed in 10 mL of water and centrifuged at 8000 rpm for 1 h to remove agglomerated large particles. Finally, the CDs powder was obtained followed by dialyzed (1000 Da) and lyophilized.

Prepare α-Fe_2O_3 photoanode (Fe_2O_3)

The α-Fe_2O_3 nanorods were synthesized on titanium foil after acid treatment through the one-pot hydrothermal and calcination method.[3] Briefly, the Ti foil after ultrasonic with acetone, ethanol and water for 20 min was placed in 30 mL concentrated hydrochloric acid and etched at 80 ℃ for 40 min, subsequently washed with deionized water several times. Then, a piece of etched Ti foil and 60 mL mixed solution which contains 1.215 g $FeCl_3 \cdot 6H_2O$, 0.27 g urea, and 10 μL $TiCl_3$ solution (15-20 wt% in HCl) were placed in a 100 mL Teflon reactor and heated at 100 °C for 10 h in an oven. After cooling down to room temperature naturally, the Ti foil were rinsed with deionized water and ethanol several times. Finally, the Ti-doped α-Fe_2O_3 photoanode (marked as Fe_2O_3 except for other statements) was obtained followed by calcination at 550 ℃ for 2 h in the muffle furnace.

Prepare modified Fe_2O_3 photoanode (Fe_2O_3/NiCo-P(CDs))

The CDs solution (10 $mg \cdot mL^{-1}$) was smeared on the surface of the Fe_2O_3 nanorods by a spin coating method at 2000 rpm for 30 s, and then calcined at 250 °C for 1 h in Ar atmosphere. Subsequently, the film was immersed in 10 mM of $CoSO_4 \cdot 7H_2O$ and $NiSO_4 \cdot 6H_2O$ (molar ratio= 3:1) aqueous solution for 1 h. And then followed by phosphating in a tube furnace immediately which contained 1.5 g of $NaH_2PO_2 \cdot H_2O$ and heated at 350 °C for 2 h under Ar atmosphere. Finally, the Fe_2O_3/NiCo-P(CDs) photoanode was obtained after being washed with water and dried overnight at 80 ℃. The Fe_2O_3/NiCo-P samples were prepared in the same way except no CDs were added.

Characterization

The morphology of these as-prepared samples was observed by a filed-emission scanning electron microscope (SU8020, 1 kV). Transmission electron microscopy (TEM) images and elemental distributions (EDS) were conducted on Field-emission transmission electron microscope (Tecnai TF20, 200 kV). The crystal structures of these films were determined by X-ray diffractometer with Cu Kα radiation (Smartlab-SE, 40 kV). X-ray photoelectron spectroscope

(XPS) results were carried out by ESCALAB 250Xi. The Fourier transform infrared spectra (FT-IR) were recorded on the Bruker V70 FT-IR spectrometer. Raman spectra were recorded via a laser Raman microscope system with the 532 nm laser source (LabRAM HR Evolution). UV-vis diffuse reflectance spectra were collected from UV-2550 (Shimadzu) spectrometer with $BaSO_4$ as the reference. The transient absorption spectra (TAS) of these samples were recorded from Laser flash photolysis spectrometer (LP980, Edinburgh) with the 355 nm laser source. The photoluminescence (PL) spectra were tested on F-7000 fluorescence spectrophotometer (Hitachi) under laser excitation of 400 nm.

Photoelectrochemical measurements

All Photoelectrochemical experiments were conducted on an electrochemical workstation (CHI 760E, CH Instrument) in 1 M KOH electrolyte (pH=13.6) under the irradiation (100 $mW \cdot cm^{-2}$) by 300 W solar simulator (Beijing Perfect light Technology Co. Ltd.) equipped with air mass (AM) 1.5G filter. The prepared films as the working electrode, Pt plate as the counter electrode, and saturated Ag/AgCl (saturated KCl) as the reference electrode. The electrode potentials of all working electrodes were converted into reversible hydrogen electrode (RHE) potentials by the Nernst equation: $E_{RHE} = E_{Ag/AgCl} + E_{Ag/AgCl}^{\theta} + 0.0591 \times pH$ ($E_{Ag/AgCl}^{\theta}$=0.1976 V at room temperature). Photo-current density applied potential (J-V) curves were determined from 0.6 V to 1.6 V_{RHE} at a scan rate of 10 $mV \cdot s^{-1}$. Electrochemical impedance spectroscopy (EIS) measurements were performed at a frequency range of 10^{-1} Hz to 10^{5} Hz with a small AC amplitude of 10 mV under 0.73 V_{RHE} bias voltage. Mott-Schottky plots were determined using the same electrochemical configuration and electrolyte in the dark, sweeping from -0.1 V to 0.2 $V_{Ag/AgCl}$ with 50 mV incensement and 1000 Hz frequency. Cyclic voltammetry (CV), carried out in 1 M KOH electrolyte with different scan rates, was employed for measuring the double capacitance (C_{dl}) of the working electrodes. The anodic-cathodic current density and the scan rate were extracted from the CV curves and fitted into a linear relationship, and the slop was C_{dl}, and the electrochemical active surface area (ECSA) was defined as $2C_{dl}$.

The dielectric constant of 80 for hematite was used to calculate the donor density following equation:

$$N_d = \frac{2}{e\varepsilon\varepsilon_0}\left[\frac{dV)}{d(1/C^2)}\right]$$

Where N_d is the donor concentration, e = 1.60 × 10^{-19} C is the electron charge, ε_0 = 8.85 × 10^{-14} F cm^{-1} is the vacuum permittivity, C is the capacitance of the space charge region, and V is the electrode applied potential.

Faradic efficiency (η_F) is used to evaluate the selectivity during the water splitting process. The η_F is defined as the ratio of the charges used for hydrogen evolution (N_F) and the overall charge flow through the external circuit (N_T).

$$\eta_F = \frac{N_F}{N_T} \times 100\%$$

2. Supplemental Figures and discussions

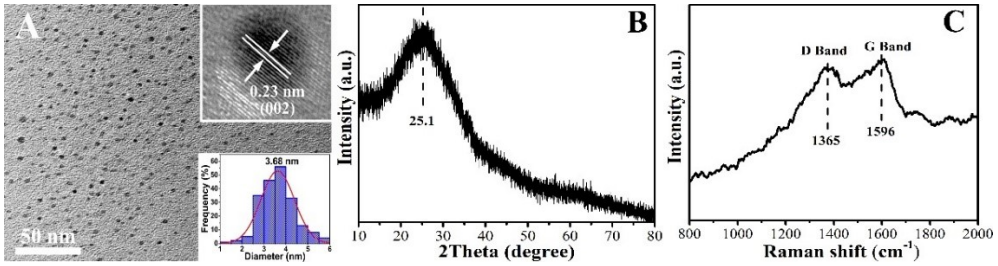

Fig. S1 (A) TEM images, XRD pattern (B) and (C) Raman spectrum of CDs.

Additional discussions

As displayed in TEM images (Fig. S1A), CDs were uniformly distributed, no aggregation of the nanoparticles can be observed, and the particle sizes range from 1 to 6 nm with a mean size of 3.68 nm. A broad diffraction peak at 25.1° was found in the XRD pattern of CDs (Fig. S1B) which is attributable to the diffraction peak of the (002) crystal plane, suggesting the crystal structure of graphite exists in CDs. Fig. S1C shows relatively weak peaks around 1365 and 1596 cm^{-1}, attributed to the D band and G band of graphitic, respectively. The D band represents the sp3 disorder carbon and the G band represents the sp2 graphite carbon in the CDs.

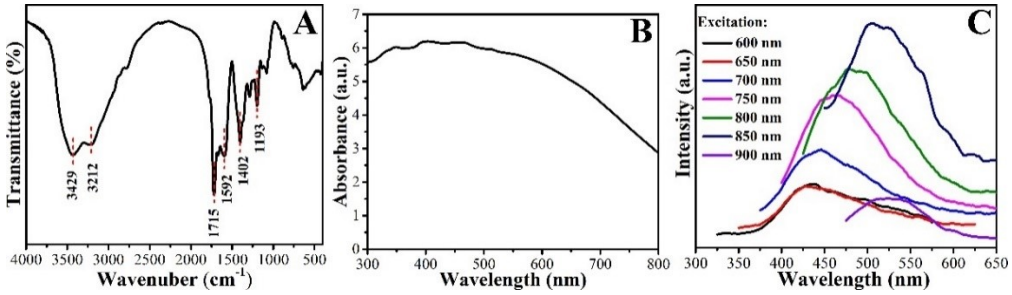

Fig. S2 (A) FT-IR, UV-vis diffuse-reflectance spectrum (B) and (C) up-conversion fluorescence spectra of CDs.

Additional discussions

In the FT-IR spectrum of CDs (Fig. S2A), the peaks located at 3429 and 3212 cm^{-1} were attributed to stretching vibration of N-H or O-H, and the absorption peaks at 1715, 1592, 1402 and 1193 cm^{-1} can be due to the C=O stretching vibrations, C-N stretching vibrations, O-H, and C-H deformation vibrations, respectively, implying that the surfaces of CDs were modified by the carboxyl, hydroxyl and amino groups. The results of UV-vis diffuse reflectance (Fig. S2B) and PL spectra (Fig. S2C) shown that CDs have strong absorption in the full wavelength range from ultraviolet to infrared region, and have obvious up-conversion fluorescence properties, which

indicate that CDs can pass through the multiphoton process to converting absorbed lower energy and longer wavelength light (>600 nm) into higher energy light with a shorter wavelength range from 400 to 550 nm, benefiting for the photochemical reaction.

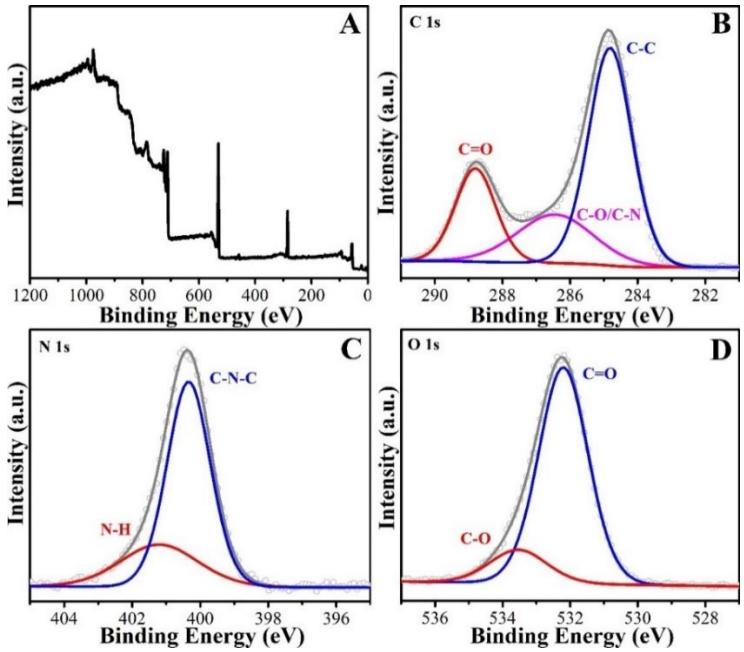

Fig. S3 (A) The survey, C 1s (B), N 1s (C) and (D) O 1s XPS spectra of CDs.

Additional discussions

The XPS survey spectrum (Fig. S3A) further discloses the surface information about CDs and proves the result from FT-IR. The specific surface groups can be reflected in terms of the deconvoluted peaks in high-resolution XPS C1s, N1s, and O1s spectra (Fig. S3B-D). The C 1s spectrum can be deconvolved into three characteristic peaks located at 288.8, 286.5, and 284.8 eV which are attributed to C=O, C-O, and C-C bonds, respectively. The peaks located at 400.3 and 401.2 eV in the N 1s spectrum were classified as N-H and C-N-C bonds, respectively. The O 1s spectrum shows two peaks located at 532.2 and 533.5 eV attributed to C=O and C-O bonds on the surface of CDs.

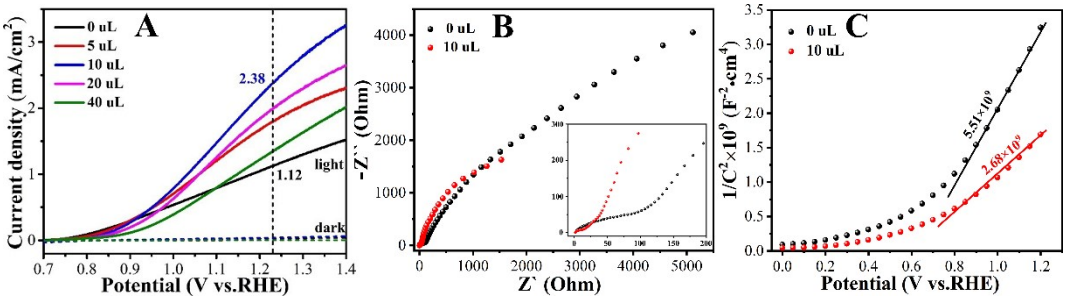

Fig. S4 (A) LSV curves of α-Fe_2O_3-based photoanodes prepared by adding various volumes of $TiCl_3$; (B) EIS plots and (C) M-S curves of α-Fe_2O_3-based photoanodes with 0 uL or 10 uL of

$TiCl_3$.

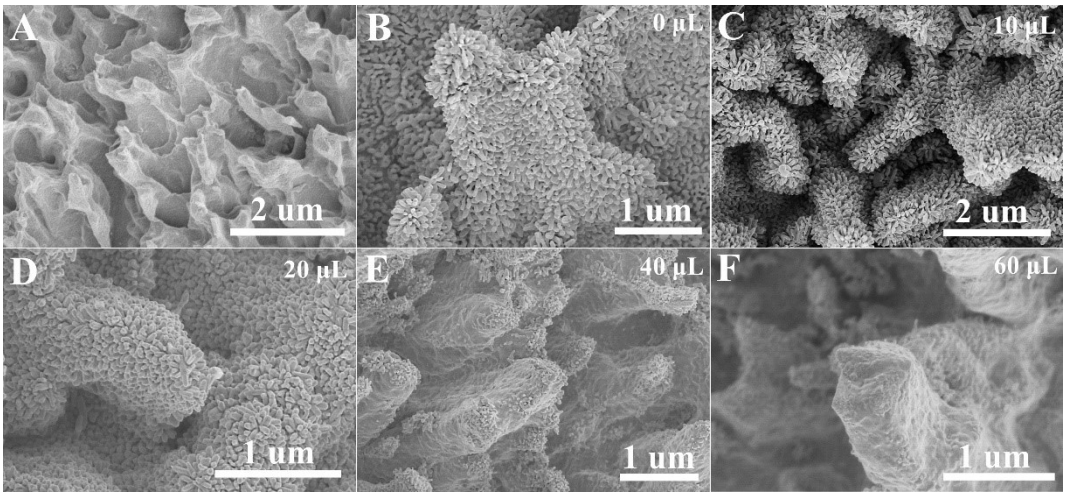

Fig. S5 (A) SEM images of Ti foil etched by hydrochloric acid and (B-F) α-Fe_2O_3-based photoanodes prepared by adding various volume of $TiCl_3$: (B) 0 uL, (C) 10 uL, (D) 20 uL, (E) 40 uL and 60 uL (F).

Additional discussions

The precursor FeOOH was converted into Fe_2O_3 by the release of H_2O during the annealed treatment at 500℃, and the fabrication process is illustrated as follows: [4-6]

$2FeOOH \rightarrow Fe_2O_3 + H_2O\ (723K)$

As shown in Fig. S4. Ti doping can effectively increase the photocurrent density, and the TFO sample corresponding to the addition of 10 μL of $TiCl_3$ shows the highest photocurrent density at 1.23 V_{RHE} (2.38 mA/cm^2), more than two times higher than the sample without Ti doping (1.12 mA/cm^2), accompanying by a decreased slope of M-S curves and Nyquist radius which reflects the increased carrier concentration and decreased charge transfer impedance. Too much addition of $TiCl_3$ (>10 μL) was not conducive to the improvement of photoanode performance (For brevity, hematite with 10 uL $TiCl_3$ addition was labeled as Fe_2O_3 except other statements).

After being etched by hydrochloric acid, the surface of the Ti foil becomes uneven with many raised microstructures similar to stone forests (Fig. S5A). During the hydrothermal reaction, hematite nanorods grow uniformly on the surface of the ravine-shaped Ti foil. A small amount of $TiCl_3$ does not significantly affect the growth of hematite nanorods, but with the increasing concentration of $TiCl_3$, the hematite nanorods gradually become shorter and even disappear (Fig. S5B-F). So, the excessive amount of $TiCl_3$ in the reaction solution was not conducive to the growth of hematite nanorods on Ti foil, which was consistent with the PEC performance results.

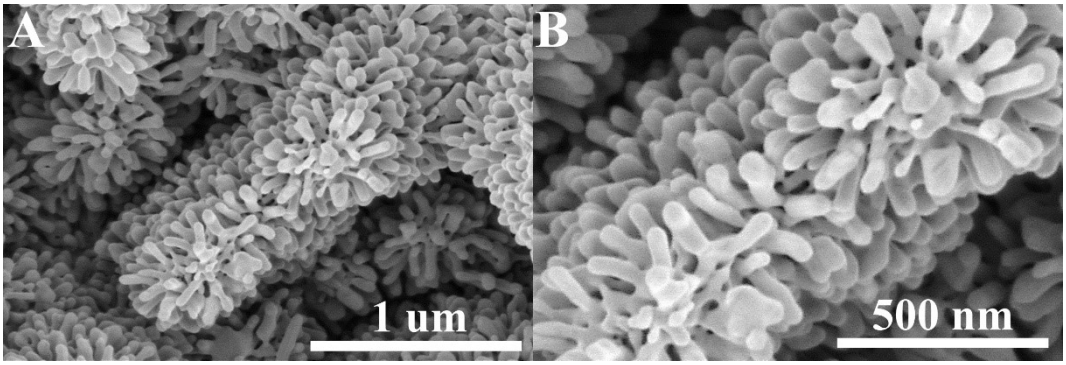

Fig. S6 SEM images of Fe_2O_3 photoanode.

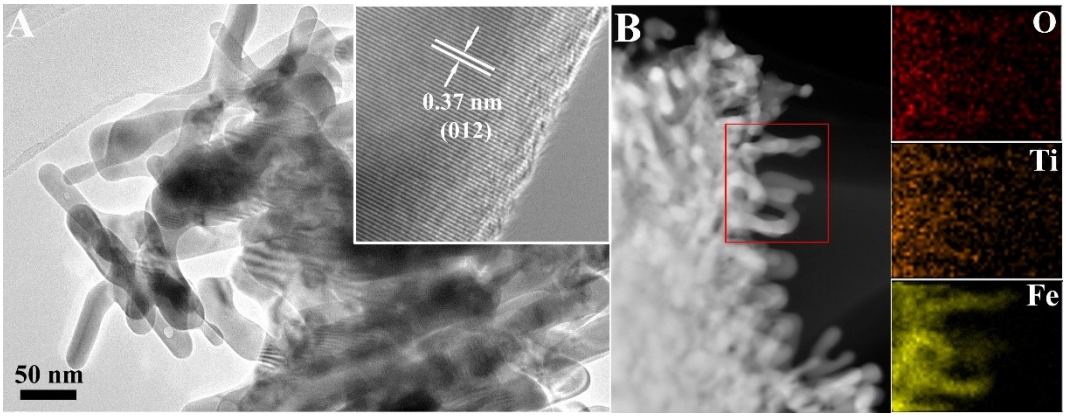

Fig. S7 (A) TEM images and (B) EDS mapping images of Fe_2O_3 photoanode.

Additional discussions

As shown in Fig. S7A, the surface of hematite nanorods was very smooth, and the crystal stripes of (012) planes with a spacing of 0.37 nm extend to the edge of the nanorods, indicating there were no other impurities in the hematite crystal phase, and the crystal structure of hematite was not affected by evenly doped Ti. The EDS mapping results showed that Ti was uniformly doped into the Fe_2O_3 nanorods (Fig. S7B).

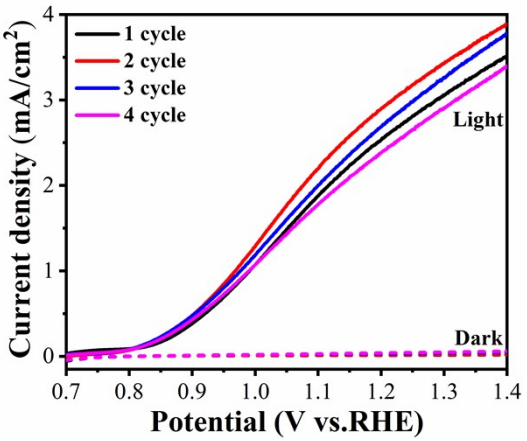

Fig. S8 LSV curves of Fe_2O_3/CDs photoanodes prepared by different spin coating times.

Additional discussions

As shown in Fig. S8, the load of CDs slightly improves the PEC performance of hematite photoanode. Considering the effect of CDs on NiCo-P catalyst layer, spin coating was selected for 3 times for subsequent experiments.

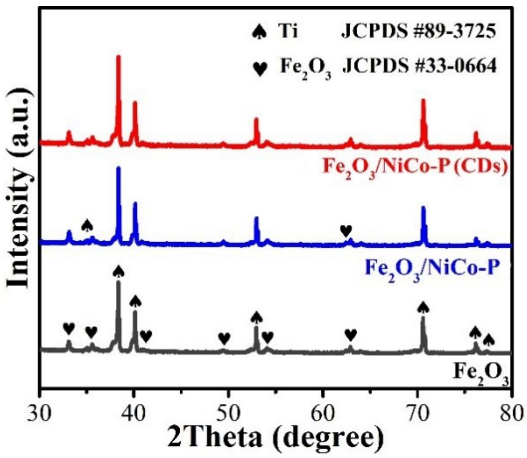

Fig. S9 The XRD patterns of prepared Fe_2O_3, Fe_2O_3/NiCo-P and Fe_2O_3/NiCo-P(CDs) photoanodes.

Additional discussions

As shown in Fig. S9, there is no significant difference in the XRD pattern of Fe_2O_3, Fe_2O_3/NiCo-P and Fe_2O_3/NiCo-P(CDs) samples, all these photoanodes could be mainly indexed into hematite (JCPDS 33-0664) and titanium (JCPDS 89-3725), and no evident peaks for CDs or NiCo-P could be detected in these XRD patterns, which should be attributed to their ultra-thin amorphous structure as well as the low amount. In addition, the loads of Fe, Co and Ni per square centimeter were measured by inductively coupled plasma emission spectroscopy (ICP) and were 4.6×10^{-1}, 3.8×10^{-3} and 1.3×10^{-3} mg, respectively.

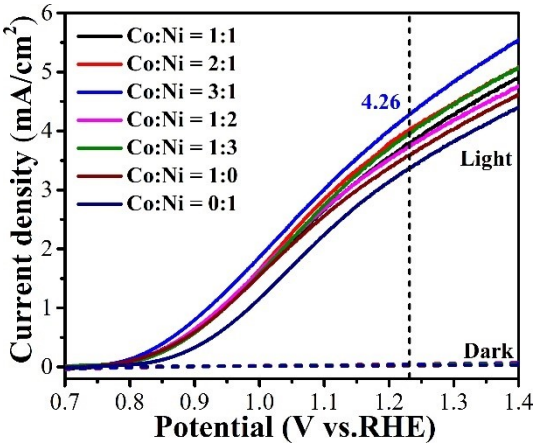

Fig. S10 LSV curves of Fe_2O_3/NiCo-P(CDs) photoanodes prepared by different mole ratios of Co and Ni.

Additional discussions

As reported by previous literatures, Ni plays an indispensable role in composite photoelectrodes. As shown in Fig. S10, compared with single Co- or Ni-based catalyst, the Fe_2O_3 photoanode decorated with NiCo bimetallic catalyst exhibited a higher photocurrent density, confirming the synergistic effect between Co and Ni for prompting water oxidation activity.

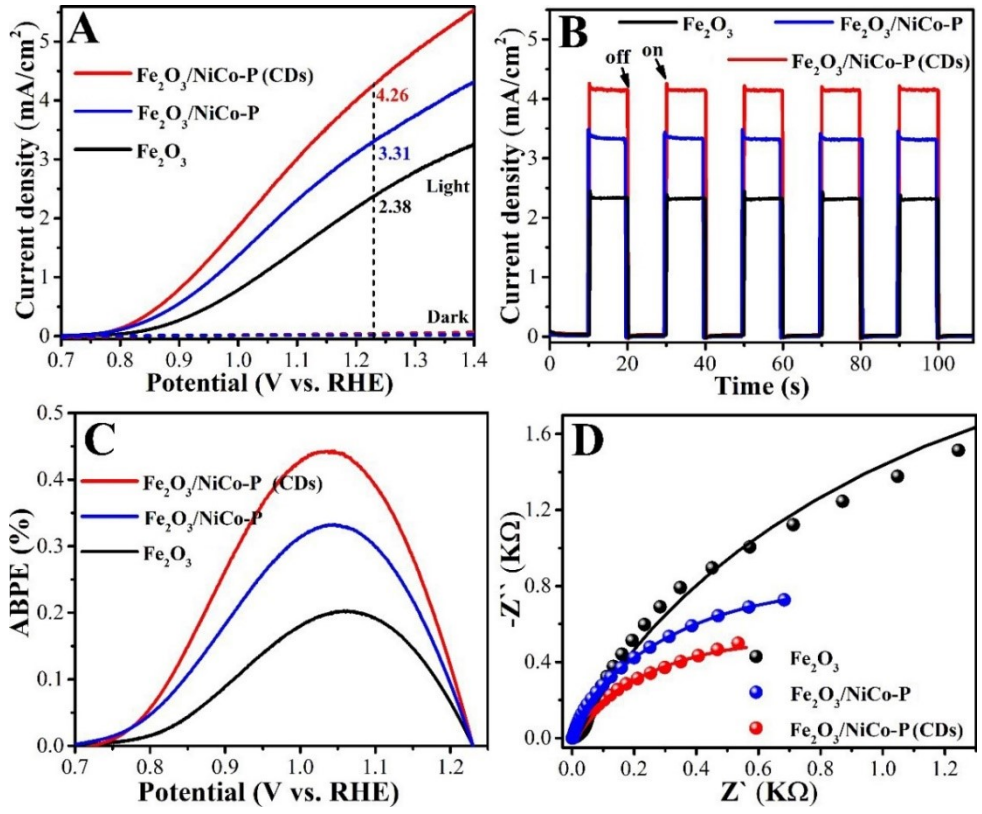

Fig. S11 (A) LSV curves, current-time curves (B), ABPE curves (C) and (D) EIS plots of Fe_2O_3,

Fe_2O_3/NiCo-P and Fe_2O_3/NiCo-P(CDs) photoelectrodes.

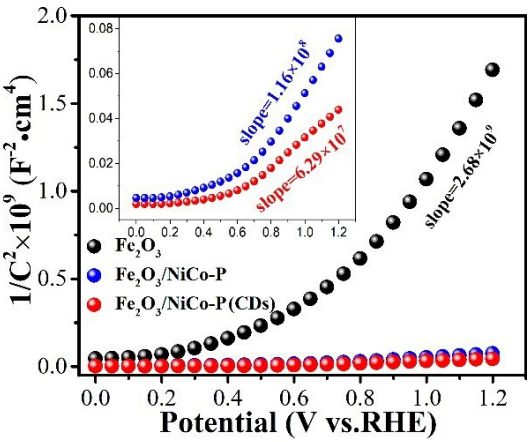

Fig. S12 Mott-Schottky curves of Fe_2O_3, Fe_2O_3/NiCo-P and Fe_2O_3/NiCo-P(CDs) photoanodes.

Additional discussions

As shown in Fig. S12, The Mott-Schottky curves of Fe_2O_3 photoanode display the highest slope compared with Fe_2O_3/NiCo-P and Fe_2O_3/NiCo-P(CDs) photoanodes, meaning the lowest carrier concentration of Fe_2O_3 photoanodes (Table S1) and worst electrical conductivity.

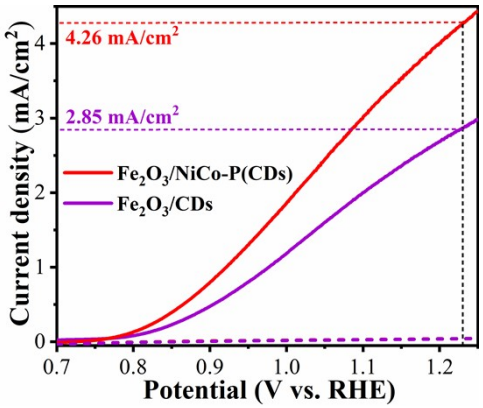

Fig. S13 The LSV curves of Fe_2O_3/CDs and Fe_2O_3/NiCo-P(CDs) photoanodes.

Additional discussions

As shown in Fig. S13, Fe_2O_3/CDs photoanode exhibited a relatively low photocurrent density of 2.85 mA/cm^2 (1.23 V_{RHE}), which is lower than that of both Fe_2O_3/NiCo-P(CDs) (4.26 mA/cm^2) and Fe_2O_3/NiCo-P (3.31 mA/cm^2), indicating that the single-decoration of CDs on Fe_2O_3 photoanodes could not significantly improve the PEC water oxidation activity.

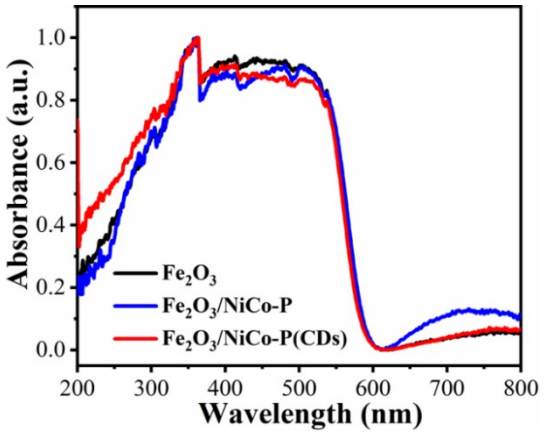

Fig. S14 UV-vis absorbance spectra of prepared photoanodes.

Additional discussions

As Fig. S14 shown, the absorption band edge at approximately 600 nm corresponds to the 2.1 eV band gap of Fe_2O_3. The UV-vis spectra of these samples did not change significantly, indicating the light absorption properties of Fe_2O_3 photoanode was not obviously affected by CDs and NiCo-P.

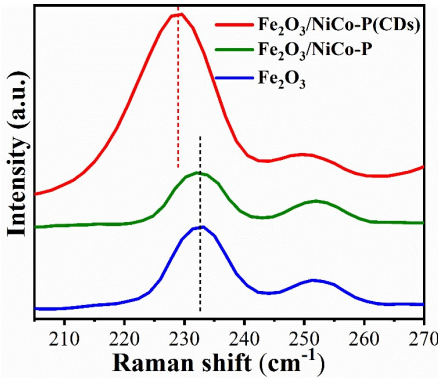

Fig. S15 The magnified Raman spectra of prepared Fe_2O_3, Fe_2O_3/NiCo-P and Fe_2O_3/NiCo-P(CDs) photoanodes.

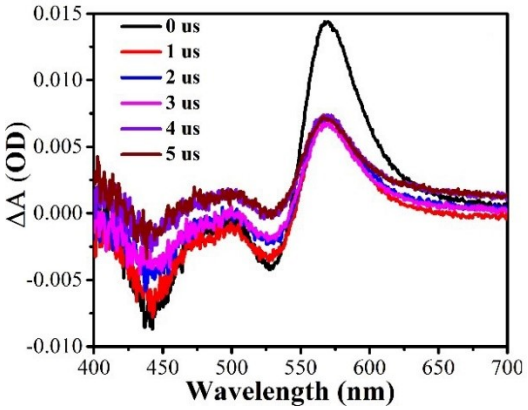

Fig. S16 TAS spectra of Fe_2O_3 recorded from 0 to 5 us after laser excitation.

Additional discussions

In the TAS spectra of Fe_2O_3 (Fig. S16), a broad positive absorption was observed from 525 to 700 nm, which was assigned to the absorption of photogenerated holes for Fe_2O_3. The negative absorption peaks at 440 and 525 nm were attributed to state filling induced bleach of the ground state absorption band.

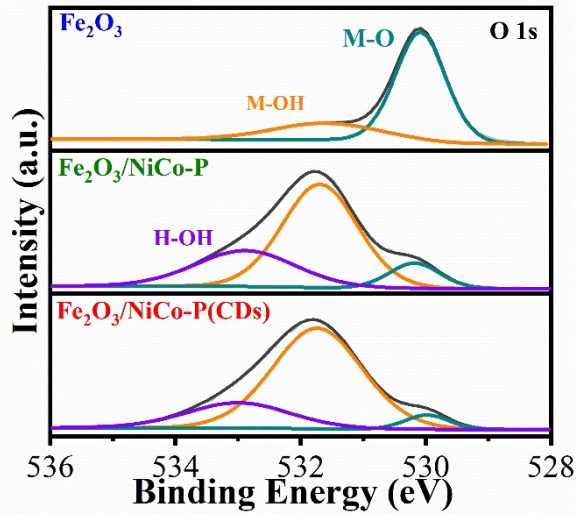

Fig. S17 The O 1s spectra of Fe_2O_3, Fe_2O_3/NiCo-P and Fe_2O_3/NiCo-P(CDs) photoanodes.

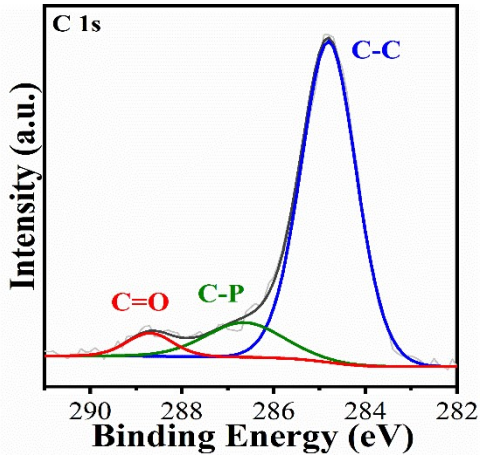

Fig. S18 The high-resolution XPS spectra of C 1s on Fe_2O_3/NiCo-P(CDs) photoanode.

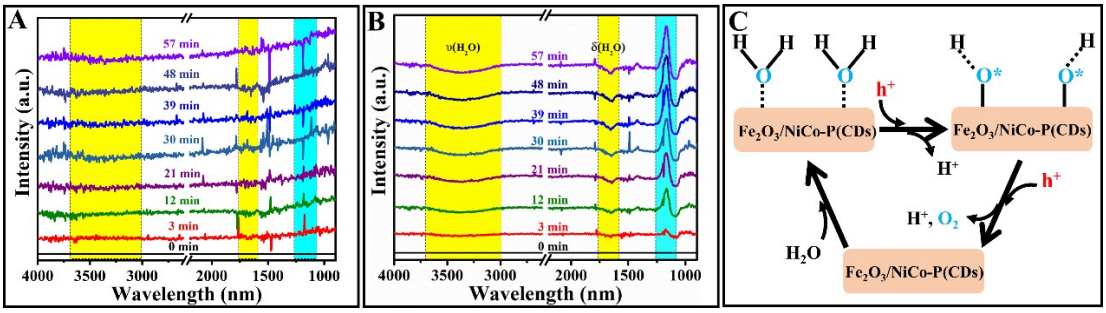

Fig. S19 (A) The in-situ FT-IR spectra of Fe_2O_3 and (B) Fe_2O_3/NiCo-P(CDs) photoanodes under light irradiate with different time. (C) Schematic diagram of the dissociation process of water molecules on the Fe_2O_3/NiCo-P(CDs) photoanode surface.

Additional discussions

The in-situ Fourier transform infrared spectroscopy (FT-IR) was adopted to explore the water molecule dissociation. As shown in Fig. S19A, it can be clearly observed that no evident changes of FT-IR peaks could be detected on the pristine Fe_2O_3 photoanodes with increasing light-irradiation time, indicating their relatively poor dissociation capability attributed to the scarce active-sites on pristine Fe_2O_3 surfaces. However, for Fe_2O_3/NiCo-P(CDs) photoanode (Fig. S19B), the intensities of adsorbed water peaks at 3300 and 1636 cm^{-1} have been negatively increased under light-irradiation, while the FT-IR peak at 1164 cm^{-1} attributed to the superoxide active species positively increased. These results clearly indicate that compared with pristine Fe_2O_3, the adsorbed water molecules could be more easily dissociated on Fe_2O_3/NiCo-P(CDs). On the basis of the above results, a possible water oxidation process on the surfaces of Fe_2O_3/NiCo-P(CDs) has been proposed in Fig. S19C.[10-11] More specifically, under light-irradiation, the adsorbed water molecules were firstly dissociated into superoxide specie intermediates on the surface Co and Ni active-sites by photo-generated holes, subsequently transformed into oxygen molecules and desorbed from OER catalyst surfaces.

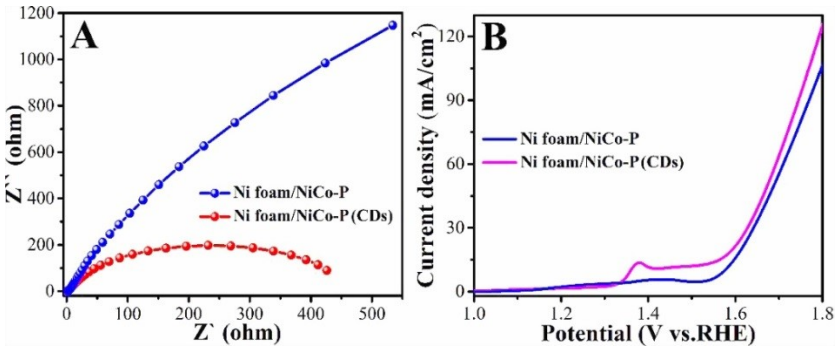

Fig. S20 (A) EIS plots and (B) LSV curves of Ni foam/NiCo-P and Ni foam/NiCo-P(CDs) photoanodes.

Additional discussions

As shown in Fig. S20, NiCo-P and NiCo-P(CDs) were loaded on the nickel foam in the same way as the preparation of Fe_2O_3/ NiCo-P(CDs) and their electrochemical properties were measured. The electrode coupled with CDs showed better electrochemical performance, indicating that CDs had a positive effect on NiCo-P catalyst.

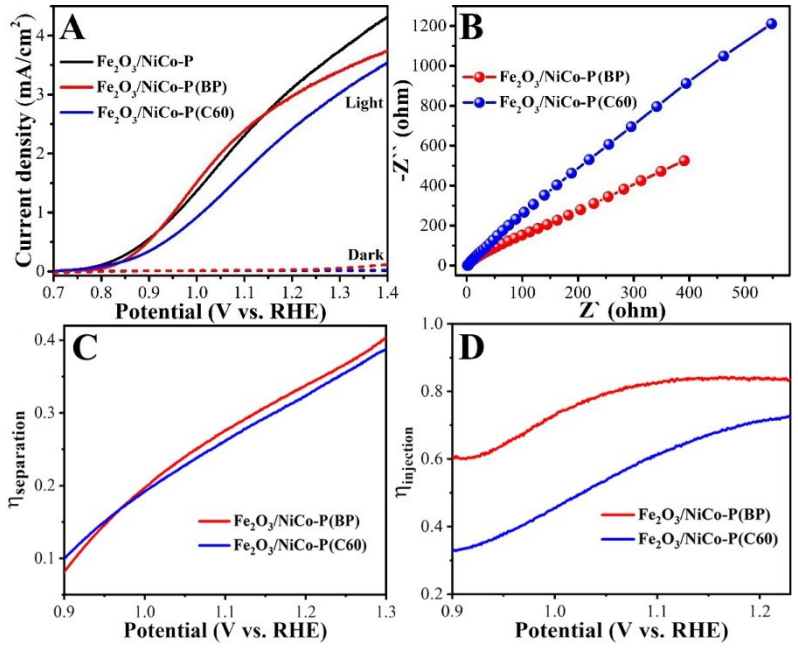

Fig. S21 (A) LSV curves, EIS plots (B), carrier separation efficiency (C) and (D) carrier injection efficiency of Fe_2O_3/NiCo-P(BP) and Fe_2O_3/NiCo-P(C60) photoanodes.

Additional discussions

As shown in Fig. S21, Black phosphorus quantum dots (BP) and C60 were used to replace CDs and were coupled with NiCo-P to prepare the composite photoanodes. Systematic PEC test results show that CDs has a unique effect on improving the PEC performance of Fe_2O_3/NiCo-P photoanode.

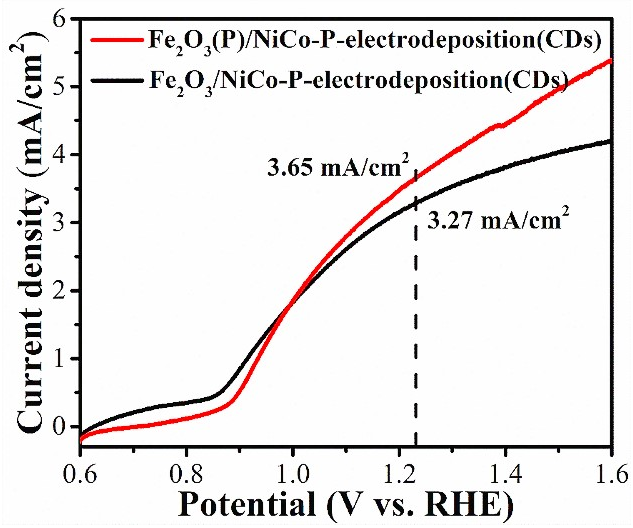

Fig. S22 LSV curves of Fe_2O_3/NiCo-P(CDs) and Fe_2O_3(P)/NiCo-P(CDs) photoanodes prepared by electrodeposition.

Additional discussions

As shown in Fig. S22, compared with Fe_2O_3/NiCo-P(CDs) photoanode, the photocurrent density of the compound photoanode prepared by electrodeposition of NiCo-P catalyst layer on Fe_2O_3/CDs photoanode is lower, which is due to the stronger interaction between CDs and NiCo-P of the NiCo-P(CDs) catalyst layer grown in situ,[12] resulting in better OER activity.

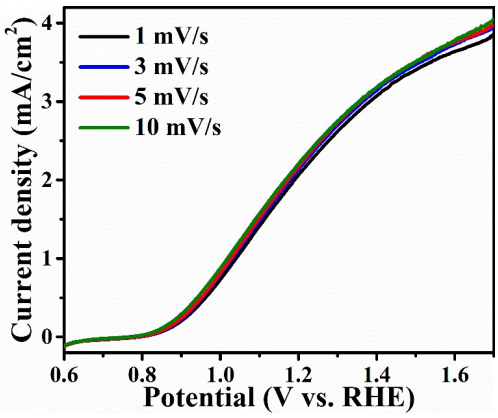

Fig. S23 LSV curves of Fe_2O_3 photoanode with different scan rates in 1 M KOH.

Additional discussions

As shown in Fig. S20, the LSV curves with a scan rate of 1 mV/s, 3 mV/s and 5 mV/s have no significant difference compare to the scan rate of 10 mV/s.

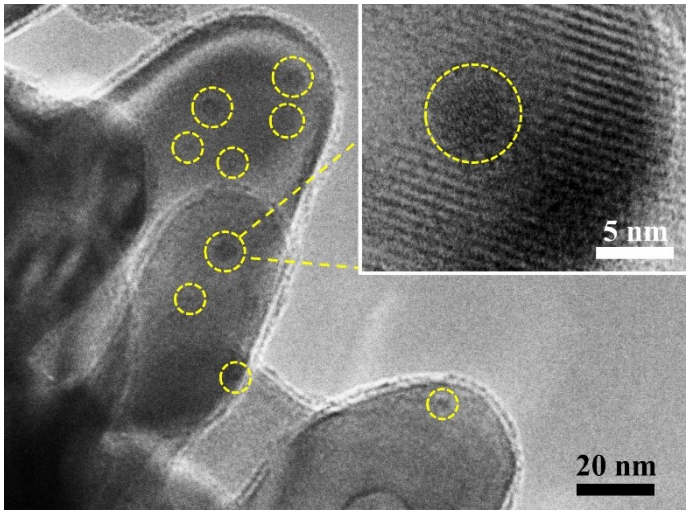

Fig. S24 TEM images of Fe_2O_3/NiCo-P(CDs) photoanode after the stability tests at 1.23 V_{RHE} for 5 hours.

Additional discussions

After the long-time measurement at high bias voltage, the blurred morphology and decreased crystallinity of CDs indicate it was maybe oxidized. In addition, it is found that the stability of photoanode can be effectively improve by reducing the applied potentials. Therefore, CDs are oxidized at high bias may be the main reason for the photoanode performance degradation.

3. Supplemental Tables

Table S1 Fitting results of the Nyquist plots and M-S plots.

Sample	R_s (Ω)	R_{trap} (Ω)	R_{ct} (Ω)	C_{bulk} (F)	C_{trap} (F)	N_d (cm^{-3})
Fe_2O_3	1.53	20.17	5396	5.61×10^{-5}	4.99×10^{-4}	6.58×10^{20}
Fe_2O_3/NiCo-P	1.56	1.99	1712	1.24×10^{-4}	4.29×10^{-4}	1.52×10^{22}
Fe_2O_3/NiCo-P(CDs)	1.34	2.19	1443	1.03×10^{-3}	3.49×10^{-4}	2.81×10^{22}

Table S2 Fitting parameters of the transient absorption kinetics.

Sample	A_1	τ_1 (ns)	A_2	τ_2 (ns)	τ_{ave} (ns)
Fe_2O_3	0.01911	33.15	0.00775	809.85	738.64
Fe_2O_3/NiCo-P	0.02467	34.10094	0.01098	847.44	780.00
Fe_2O_3/NiCo-P(CDs)	0.01415	40.18	0.00716	895.11	825.45

Table S3 The content of each element of Fe_2O_3/NiCo-P(CDs) sample calculated by XPS results.

Elements	Co	Ni	Fe	P	O	N	C
Atomic %	5.57	2.17	4.79	9.43	48.95	3.04	26.05

Additional discussions

ICP was performed for Fe_2O_3/NiCo-P(CDs) samples, and the calculated mass of Co and Ni loads per square centimeter are 3.8×10^{-3} and 1.3×10^{-3} mg, respectively (Co/Ni=2.92). Furthermore, the element contents in the Fe_2O_3/NiCo-P(CDs) sample were also calculated by XPS results (Table. S3). It can be seen that the atomic percentage of Co and Ni are 5.57 % and 2.17 %, respectively (Co/Ni=2.57).

Table S4 Performances of the recently reported hematite-based photoanodes.

Hematite-based photoanodes	Photocurrent density ($1.23\ V_{RHE}$)	Reference
$Ti:Fe_2O_3/CoFeO_x$	2.49 mA/cm²	[13]*Adv. Funct. Mater., 26, 4414 (2016).*
$Ti:Fe_2O_3/Ti\text{-}SiO_x/Co\text{-}Pi$	3.19 mA/cm²	[14]*Angew. Chem. Int. Ed., 55, 9922 (2016)*
$Ti:Fe_2O_3/ZnFe_2O_4/Co\text{-}Pi$	3.60 mA/cm²	[15]*Applied Energy, 164, 924 (2016)*
$P:Fe_2O_3/Co\text{-}Pi$	2.00 mA/cm²	[16]*Chem. Sci., 8, 91 (2017)*
$Fe_2O_3/Fe_2TiO_5/FeNiOOH$	2.20 mA/cm²	[17]*Energy Environ. Sci., 10, 2124 (2017)*
$B,Ti,Sn:Fe_2O_3/FeOOH$	2.35 mA/cm²	[18]*ACS Catal., 8, 11932 (2018)*
$P:Fe_2O_3/NiO$	2.08 mA/cm²	[19]*Chemsuschem, 11, 2156 (2018)*
$Fe_2O_3/FeNbO_4/NiFeO_x$	2.71 mA/cm²	[20]*ACS Catalysis, 9, 1289 (2018)*
$Ti:Fe_2O_3/Co\text{-}Pi$	3.50 mA/cm²	[21]*Nat. Commun., 10, 4832 (2019)*
$Ti:Fe_2O_3/Co_3O_4/Co\text{-}Pi$	2.70 mA/cm²	[22]*Adv. Funct. Mater., 29, 1801902 (2019)*
$Fe_2O_3/Al_2O_3/CoFeOx$	2.50 mA/cm²	[23]*J. Mater. Chem. A, 7, 6012 (2019)*
$Fe_2O_3/CoAl\text{-}LDH$	2.46 mA/cm²	[24]*ACS Appl. Mater. Inter., 11, 29799 (2019)*
$Fe_2O_3/Fe\text{-}Pi$	2.71 mA/cm²	[25]*ACS Appl. Mater. Inter., 11, 22272 (2019)*
$Fe_2O_3/Co\text{-}Mn$ nanosheets	2.07 mA/cm²	[26]*Adv. Funct. Mater., 29, 1904622 (2019)*
$Fe_2O_3/FeO_xF_y/ZIF\text{-}67$	2.56 mA/cm²	[27]*Nano Energy, 78, 105396 (2020)*
$Fe_2O_3/GO/NiFeOOH$	3.10 mA/cm²	[28]*Adv. Funct. Mater., 30, 2002124 (2020)*
$F:Fe_2O_3/FeOOH/CoOOH$	2.34 mA/cm²	[29]*ACS Appl. Mater. Inter., 12, 49705 (2020)*
$Ta:Fe_2O_3/NiFe(OH)_x$	3.22 mA/cm²	[30]*Nat. Commun., 11, 4622 (2020)*
Fe_2O_3/MoO_x	2.60 mA/cm²	[31]*Appl. Catal. B: Environ., 284, 119760 (2021)*
$Fe_2O_3/MXene$	1.10 mA/cm²	[32]*Appl. Catal. B: Environ., 291, 120107 (2021)*
$Fe_2O_3/NiCo\text{-}P(CDs)$	**4.26 mA/cm²**	***This work***

4. Supplementary References

1 Y. Wang, X. Liu, X. Han, R. Godin, J. Chen, W. Zhou, C. Jiang, J. F. Thompson, K. B. Mustafa, S. A. Shevlin, J. R. Durrant, Z. Guo and J. Tang, *Nat. Commun.*, 2020, **11**, 2531.

2 S. Qu, X. Wang, Q. Lu, X. Liu and L. Wang, *Angew. Chem. Int. Ed.*, 2012, **51**, 12215-12218.

3 C. Feng, S. Fu, W. Wang, Y. Zhang and Y. Bi, *Appl. Catal. B-Environ.*, 2019, **257**, 117900.

4 K. Cao, L. Jiao, H. Liu, Y. Liu, Y. Wang, Z. Guo and H. Yuan, A*dv. Energy Mater.*, 2015, **5**, 1401421.

5 J. Xie, P. Yang, X. Liang and J. Xiong, *ACS Appl. Energy Mater.*, 2018, **1**, 2769-2775.

6 X. Wang, X. Chen, L. Gao, H. Zheng, M. Ji, C. Tang, T. Shen and Z. Zhang, *J. Mater. Chem. A*, 2004, **14**, 905-907.

7 L. Wang, J. Zhu, X. Liu, *ACS Appl. Mater. Interfaces*, 2019, **11**, 22272-22277.

8 H. Liang, C. Xia, A. H. Emwas, D. H. Anjum, X. Miao and H. N. Alshareef, *Nano Energy*, 2018, **49**, 155-162.

9 Y. Wei, X. Li, Q. Liu, Y. Zhang, K. Zhang, P. Huo and Y. Yan, *Carbon*, 2022, **188**, 59-69.

10 Y. Zhang, H. Zhang, A Liu, C. Chen, W. Song and J. Zhao, *J. Am. Chem. Soc.*, 2018, **140**, 3264-3269.

11 H. Sheng, H. Zhang, W. Song, H. Ji, W. Ma, C. Chen and J. Zhao, *Angew. Chem. Int. Ed.*, 2015, **54**, 5905-5909.

12 T. Li, Q. Zhou, J. Qian, Y. Hu and Y. Zheng, *Electrochim. Acta*, 2019, **307**, 92-99.

13 Y. F. Xu, X. D. Wang, H. Y. Chen, D. B. Kuang and C. Y. Su, *Adv. Funct. Mater.*, 2016*,* **26**, 4414-4421.

14 H. J. Ahn, K. Y. Yoon, M. J. Kwak and J. H. Jang, *Angew. Chem. Int. Ed.*, 2016, **55**, 9922-9926.

15 Y. J. Chen and L. Y. Chen, *Applied Energy*, 2016, **164**, 924-933.

16 Z. Luo, C. Li, S. Liu, T. Wang and J. Gong, *Chem. Sci.*, 2017, **8**, 91-100.

17 P. Tang, H. Xie, C. Ros, L. Han, M. Biset-Peiro, Y. He, W. Kramer, A. P. Rodriguez, E. Saucedo, J. R. Galan-Mascaros, T. Andreu, J. R. Morante and J. Arbiol, *Energy Environ. Sci.*, 2017, **10**, 2124-2136.

18 H. J. Ahn, K. Y. Yoon, M. J. Kwak, J. Park and J. H. Jang, *ACS Catal.*, 2018, **8**, 11932-11939.

19 F. Li, J. Li, J. Zhang, L. Gao, X. Long, Y. Hu, S. Li, J. Jin and J. Ma, *Chemsuschem*, 2018, **11**, 2156-2164.

20 H. Zhang, Y. K. Kim, H. Y. Jeong and J. S. Lee, *ACS Catal.*, 2019, **9**, 1289-1297.

21 Z. Zhang, I. Karimata, H. Nagashima, S. Muto, K. Ohara, K. Sugimoto and T. Tachikawa, *Nat. Commun.*, 2019, **10**, 1-2.

22 S. S. Yi, B. R. Wulan, J. M. Yan and Q. Jiang, *Adv. Funct. Mater.*, 2019, **29**, 1801902.

23 L. Liardet, J. E. Katz, J. Luo, M. Gratzel and X. Hu, *J. Mater. Chem. A*, 2019, **7**, 6012-6020.

24 C. Wang, X. Long, S. Wei, T. Wang, F. Li, L. Gao, Y. Hu, S. Li and J. Jin, *ACS Appl. Mater. Inter.*, 2019, **11**, 29799-29806.

25 L. Wang, J. Zhu and X. Liu, *ACS Appl. Mater. Inter.*, 2019, **11**, 22272-22277.

26 G. Yang, Y. Li, H. Pang, K. Chang and J. Ye, *Adv. Funct. Mater.*, 2019, **29**, 1904622.

27 S. Chen, J. Bai, X. Nurimaimaiti, J. Wang, Y. Zhang, T. Zhou, J. Li and B. Zhou, *Nano Energy*, 2020, **78**, 105396.

28 A. Kormanyos, E. Kecsenovity, A. Honarfar, T. Pullerits and C. Janaky, *Adv. Funct. Mater.*, 2020, **30**, 2002124.

29 T. Wang, X. Long, S. Wei, P. Wang, C. Wang, J. Jin and G. Hu, *ACS Appl. Mater. Inter.*, 2020, **12**, 49705-49712.

30 H. Zhang, D. Li, W. J. Byun, X. Wang, T. J. Shin, H.Y. Jeong, H. Han, C. Li and J. S. Lee, *Nat. Commun.*, 2020, **11**, 4622.

31 H. M. Li, Z. Y. Wang, H. J. Jing, S. S. Yi, S. X. Zhang, X. Z. Yue, Z. T. Zhang, H. X. Lu and D. L. Chen, *Appl. Catal. B-Environ.*, 2021, **284**, 119760.

32 R. K. Ye, S. S. Sun, L. Q. He, S. R. Yang, X. Q. Liu, P. P. Fang and J. Q. Hu, *Appl. Catal. B-Environ.*, 2021, **291**, 120107.